Open Access

This article is licensed under CC-BY-NC-ND 4.0

ARTICLE

Hybrid Aeromaterials for Enhanced and Rapid Volumetric Photothermal Response

Lena M. Saure, Niklas Kohlmann, Haoyi Qiu, Shwetha Shetty, Ali Shaygan Nia, Narayanan Ravishankar, Xinliang Feng, Alexander Szameit, Lorenz Kienle, Rainer Adelung, and Fabian Schütt*

Read Online

ACCESS | Metrics & More | Article Recommendations | SI Supporting Information

ABSTRACT: Conversion of light into heat is essential for a broad range of technologies such as solar thermal heating, catalysis and desalination. Three-dimensional (3D) carbon nanomaterial-based aerogels have been shown to hold great promise as photothermal transducer materials. However, until now, their light-to-heat conversion is limited by near-surface absorption, resulting in a strong heat localization only at the illuminated surface region, while most of the aerogel volume remains unused. We present a fabrication concept for highly porous (>99.9%) photothermal hybrid aeromaterials, which enable an ultrarapid and volumetric photothermal response with an enhancement by a factor of around 2.5 compared to the pristine variant. The hybrid aeromaterial is based on strongly light-scattering framework structures composed of interconnected hollow silicon dioxide (SiO_2) microtubes, which are functionalized with extremely low amounts (in order of a few $\mu g\ cm^{-3}$) of reduced graphene oxide (rGO) nanosheets, acting as photothermal agents. Tailoring the density of rGO within the framework structure enables us to control both light scattering and light absorption and thus the volumetric photothermal response. We further show that by rapid and repeatable gas activation, these transducer materials expand the field of photothermal applications, like untethered light-powered and light-controlled microfluidic pumps and soft pneumatic actuators.

KEYWORDS: aeromaterial, aerogel, photothermal effect, graphene, 2D nanomaterials, soft robotics, microfluidics
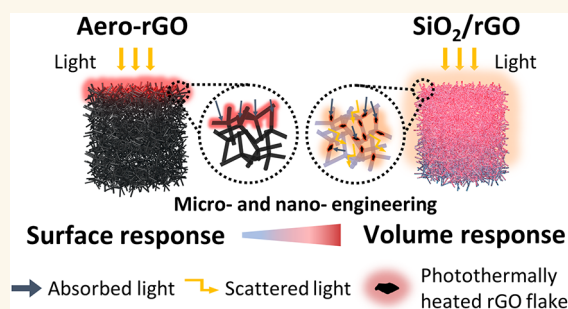
INTRODUCTION

The generation of thermal energy from light is an essential physical process that not only governs all biological processes but also is of major importance for a broad variety of technologies, ranging from fundamental environmental applications like hot water generation,[1] desalination,[1] thermal management of buildings,[2,3] power generation,[1] solar thermal heating,[4,5] catalysis[6−8] to medical applications.[9] For the conversion of light to heat, the photothermal effect is exploited, where light is absorbed by photothermal materials, resulting in a temperature rise. The photothermal efficiency, i.e., the amount of light converted to thermal energy, strongly depends on the type of material and its surface properties. Only light that is not directly reflected can be either converted into electric energy (photovoltaic effect), into another wavelength (fluorescence) or into thermal energy. The latter usually accounts for the largest part.

With respect to that, nanomaterials have been shown to hold great potential as efficient photothermal agents due to their large surface-to-volume ratio as well as their extraordinary electronic structure. Photothermal nanomaterials include semiconductor nanomaterials, plasmonic metal nanoparticles, polymer-based nanomaterials as well as carbon and related

nanomaterials, such as graphene, carbon nanotubes and MXenes.[10−13] For example, just recently, a photothermal efficiency of ~100% could be reached by utilizing Ti_3C_2 based nanomaterials.[14] Due to their small size (below 100 nm), photothermal nanomaterials have been employed as therapeutic agents for the localized heat treatment of cancer,[9] as well as in the sterilization of surfaces to prevent bacterial biofilm formation.[15]

Moreover, three-dimensional (3D) aerogels and foam structures made of the aforementioned photothermal nanomaterials have recently been shown to hold great potential as light-to-heat transducer materials. Their extremely low volumetric density (typically below 20 mg cm^{-3})[16,17] results in a volumetric heat capacity similar to that of air, enabling a rapid and efficient heating under light illumination. Simulta-
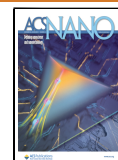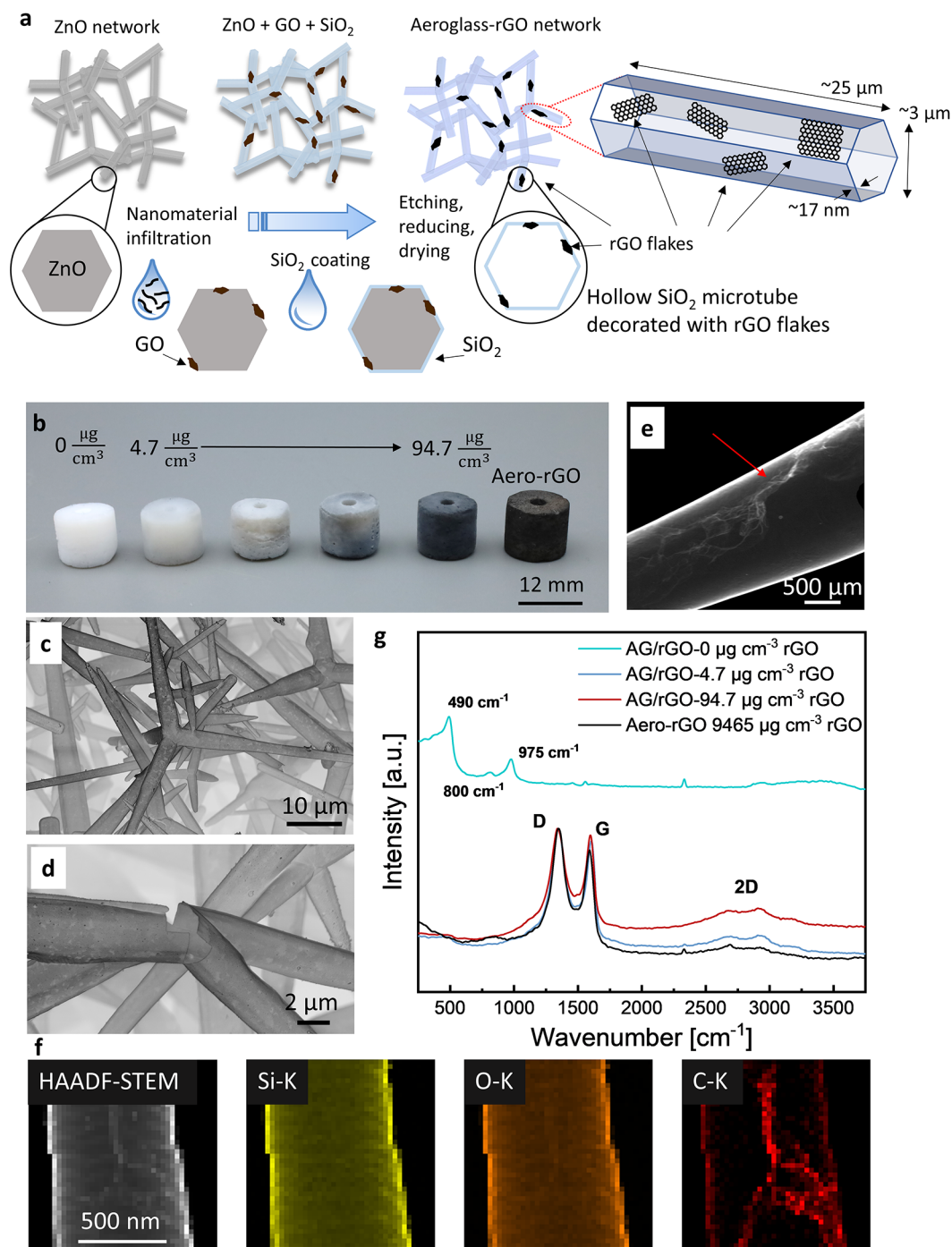
Figure 1. Synthesis and characterization of AG/rGO transducer materials. (a) Schematic of synthesis steps of aeroglass functionlized with rGO and magnified hollow microtube with rGO flakes distributed on the surface of the microtube. (b) Photograph of functionalized aeroglass (AG/rGO) samples with different volumetric loadings of rGO (c,d) SEM images of a AG/rGO-94.7 sample, revealing the open porous structure and the hollow character of microtubes with a homogeneous distribution of rGO flakes. (e) TEM image of a AG/rGO-94.7 sample showing a rGO flake on a SiO₂ microtube. (f) EDX mapping of AG/rGO-94.7 for silicon, oxygen and carbon, clearly indicating the existence of a rGO flake on a microtube. (g) Raman spectra for pristine AG, AG/rGO-4.7 and AG/rGO-94.7, as well as for Aero-rGO. The spectra clearly indicate typical peaks for D, G and 2D band for rGO.

neously, their macroscopic size, their porous structure (typically >98%)[16,17] and high surface area (up to 75 m² g⁻¹)[17] lead to a variety of light−matter interactions, including light scattering, light absorption and reflection. Their potential as an excellent material platform for light-to-heat conversion has already been demonstrated in several applications ranging from photoacoustics,[18] water steam generation,[11−13,17] hydrogen catalysis[19,20] to desalination.[1,11]

However, while these studies indicate the potential of carbon and related nanomaterial-based foams as light-to-heat transducer materials, in all reported cases the light illumination only results in a strong heat localization at the surface region of the photothermal active aerogel,[12,13,17] as the light penetration into

the macroscopic aerogel structure is physically limited. Especially, the transfer of heat to the surrounding medium, e.g., gas, which is essential for most applications, is physically limited by the low density of gases (typically 4 orders of magnitude below solids), requiring a high surface area for activation of large gas volumes.

Here we present a concept for the design and development of nano- and microengineered hybrid aeromaterial transducers with enhanced volumetric light-to-heat conversion. The concept is based on an open porous (porosity ~99.9%), ultralightweight (density ~3 mg cm^{-3}), nonabsorbing and light scattering framework structure composed of silicon dioxide (SiO$_2$) microtubes, named aeroglass (AG), functionalized with low volumetric loadings (between 4.7 μg cm^{-3} and 94.7 μg cm^{-3}) of reduced graphene oxide (rGO), acting as the photothermal agent. By utilizing the light scattering properties of the pristine AG, and tailoring the volumetric density of rGO within the AG, we show that the light penetration depth into the foams can be increased up to 10 mm, thereby increasing the photothermally activated gas volume by a factor up to 2.44 compared to a pristine rGO aeromaterial transducer, which, due to a high open porosity, already has a relatively high light penetration depth compared to conventional aerogels. We further demonstrate that these micro- and nanoengineered transducer materials enable versatile application scenarios for light-to-heat conversion, including untethered and light-driven pneumatic actuators for soft robotics, as well as wireless light-powered and -controlled microfluidic pumps.

RESULTS

Synthesis and Characterization. The synthesis process of the macroscopic nano- and microengineered transducer material is schematically shown in Figure 1a. In short, a sacrificial network of tetrapodal-shaped ZnO microparticles is first partially coated with a photothermal nanomaterial by a simple infiltration process, followed by a wet chemical SiO$_2$ coating step. Etching of ZnO and supercritical drying results in a freestanding multiscale material system (porosity >99.9%) composed of interconnected hollow SiO$_2$ microtubes decorated with photothermal nanomaterial. More details on the synthesis can be found in the Materials and Methods section. We here use reduced graphene oxide (rGO) as a light absorbing nanomaterial due to the broadband absorption of UV−vis and near-infrared range (NIR) light.[9,10,17,21] The hybrid transducer material is named AG/rGO. However, other light absorbing nanomaterials such as gold nanoparticles can be incorporated by the same method as well; see Figure S1. By adjusting the concentration of the used graphene oxide (GO) dispersion, the volumetric loading of rGO within the AG can be precisely adjusted between 0 and 94.7 μg cm^{-3}, which is key to tailoring the volumetric light−matter interaction of the system. Figure 1b shows a photograph of cylindrical AG/rGO samples with different volumetric loadings of rGO, as well as pristine AG and the pristine rGO variant, named Aero-rGO. The structural features of all aeromaterials compared in this study are similar, but in contrast to AG and AG/rGO samples, the hollow microtubes of Aero-rGO are purely composed of rGO, see Table 1 and Materials and Methods. A detailed characterization of Aero-rGO can be found in previous publications.[22,23] While pristine AG shows a white appearance, a color shift to dark gray with increasing rGO loading in the AG/rGO hybrid aeromaterial structure is observed. The optical appearance of the pristine Aero-rGO is significantly

Table 1. Types of Aeromaterials Used in This Study, All with Similar Open Porous Structure

Abbreviation	Material	Description
AG	SiO$_2$	Aeroglass, i.e., aeromaterial composed of SiO$_2$
AG/rGO-xx	SiO$_2$ and rGO	Aeroglass functionalized with reduced graphene oxide, -xx is the volumetric loading of rGO within the aeroglass structure in μg cm^{-3}
Aero-rGO	rGO	Aeromaterial composed of reduced graphene oxide

darker, as the concentration of rGO is 100 times higher (9465 μg cm^{-3}) than for the AG/rGO with highest loading of rGO (94.7 μg cm^{-3}). It has to be noted that the properties, e.g., light transport, of the aeromaterials strongly differ from those of conventional aerogels.[23,24] SEM characterization (Figure 1c, d) reveals the open porous network structure as well as the hollow character of the SiO$_2$ microtubes and clearly shows the homogeneous distribution of rGO flakes on the surface of the microtubes. A more detailed SEM characterization, including Aero-rGO, is shown in Figure S2. Individual microtubes have a mean length of ~25 μm and a diameter of ~1−3 μm. The wall thickness of the hollow microtubes was determined by TEM with an average wall thickness of ~17 nm (for more details, see Supplementary Note 1). Figure 1e shows a SiO$_2$ microtube arm decorated with an rGO flake. EDX mapping confirms the existence of rGO flakes incorporated into the SiO$_2$ layer (Figure 1f). The as-synthesized SiO$_2$ is amorphous, as determined by TEM investigations (see Figure S3). This agrees with the Raman measurements shown in Figure 1g, which were conducted for the pristine AG, pristine Aero-rGO and for the highest (AG/rGO-94.7) and lowest (AG/rGO-4.7) degrees of rGO functionalization. Typical Raman peaks for rGO are observed in both the AG/rGO hybrid material systems as well as the pristine Aero-rGO. The positions of D band (1339 cm^{-1}) and G band (1597 cm^{-1}) are in accordance with the literature, as well as the less pronounced 2D peak.[22,25−28] The Raman spectrum of the pristine AG shows distinct peaks at 490, 800 and 975 cm^{-1} which are typical for amorphous SiO$_2$ structures.[29,30]

Optimizing Volumetric Light Absorption. The as-described multiscale nature of the hybrid aeromaterials used here enables a variety of light−matter interactions, as shown in Figure 2a,b. Illuminating aeromaterial structures of pristine AG (density ~3 mg cm^{-3}) with a focused light beam results in strong isotropic light scattering in all room directions, similar to what has been previously reported for framework structures based on hexagonal boron nitride.[24] The AG acts as a volumetric light diffuser. In contrast to that, aeromaterials composed of rGO with a density of 11 mg cm^{-3} absorb all light when illuminated with a focused light beam due to their broadband absorption properties (Figure 2b). While these demonstrate the two extreme cases, either complete light scattering in the case of pristine AG or complete light absorption in the case of pristine Aero-rGO, tailoring the volumetric density of rGO inside of the AG framework structure enables us to adjust the volumetric light−matter interactions of the AG/rGO hybrid aeromaterials in a controlled manner. Figure 2c shows the light transmission through cylindrically shaped (d = 12 mm) AG/rGO hybrid aeromaterials with varying degrees of volumetric rGO density (0, 4.7 and 94.7 μg cm^{-3}) as well as Aero-rGO as a function of sample height (2−10 mm). In the case of pristine Aero-rGO, even at a sample height of 2 mm no light is transmitted through the aeromaterial structure. AG/rGO-94.7 transmits a
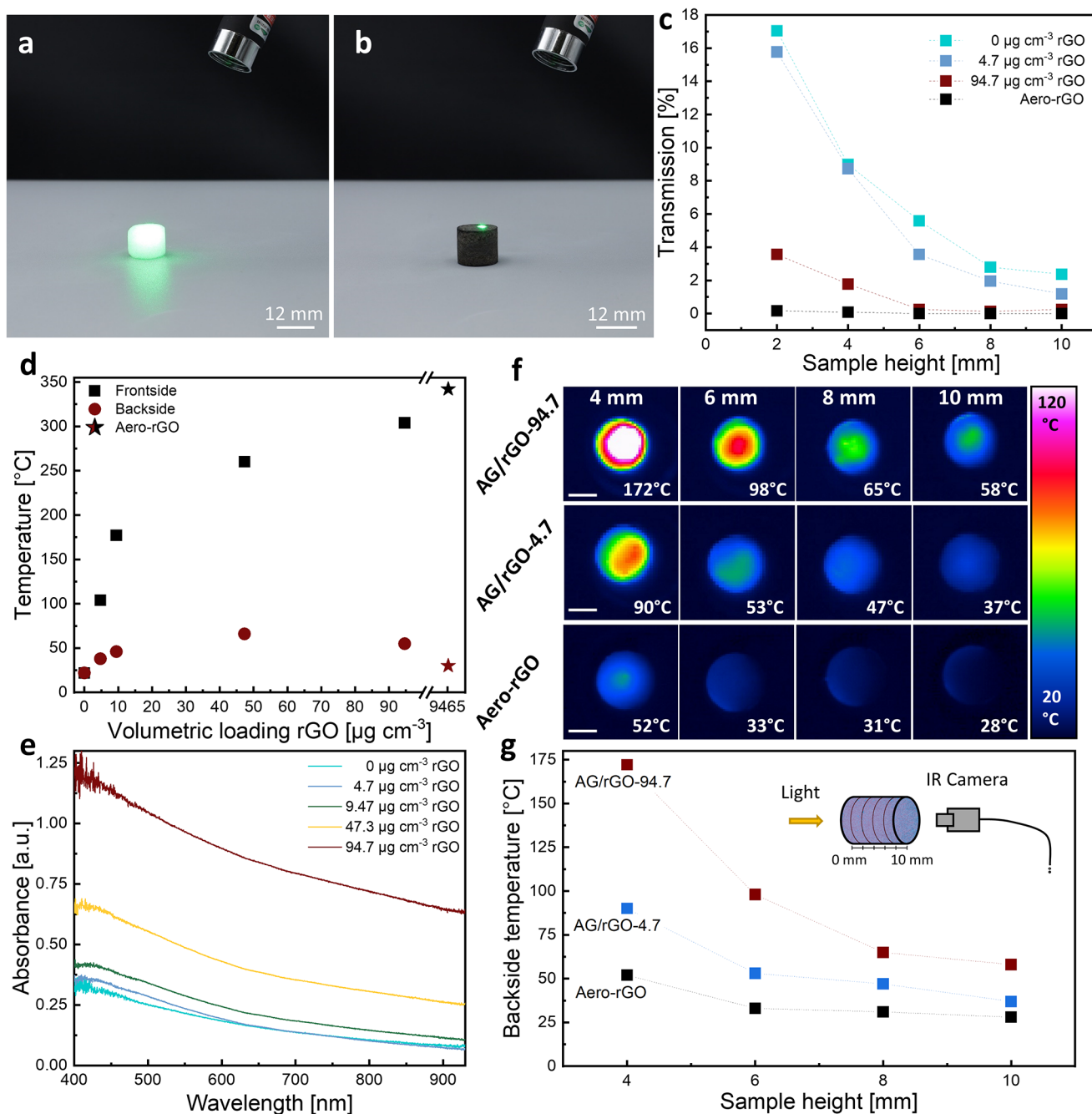
Figure 2. Light induced heating of AG/rGO. (a,b) Photograph of pristine AG and pristine Aero-rGO illuminated with a green laser pointer. (c) Light transmission of pristine AG, Aero-rGO and AG/rGO with high (94.7 μg cm^{-3}) and low (4.7 μg cm^{-3}) volumetric rGO loading measured for different sample heights. (d) Maximum temperature of AG/rGO samples with different volumetric loadings of rGO and a height of 10 mm, illuminated for 1 s with an irradiance of 1.67 W cm^{-2} extracted from IR images of frontside (illumination side) and backside. (e) UV−vis absorbance for different volumetric loadings of rGO within AG/rGO hybrid aeromaterial. (f) IR images of sample backside of AG/rGO with different volumetric rGO loadings and Aero-rGO samples with increasing sample heights, showing the temperature profile after illuminating the samples for 1 s with an irradiance of 1.67 W cm^{-2}. Scale bar is 6 mm. (g) Maximum backside temperature for different sample heights. The schematic illustrates the measurement setup.

small amount of light for sample dimension of 2 mm and 4 mm (3.5% and 1.8%), whereas the highest transmitted light intensity is detected for pristine AG with 2 mm height (17%). However, also AG/rGO-4.7 shows high light transmission for 2 mm (15.7%) which strongly decreases with increasing sample thickness. Even for 10 mm sample thickness, a small amount of transmitted light is still detected (2.4%), meaning that some light can transmit through the structure

without being absorbed by rGO. The results indicate that the volumetric density of rGO within the hybrid aeromaterial strongly influences the light penetration depth into the structure, and by this, the size of the light−matter interaction volume. This can also be visualized by thermography, as light interacting with the rGO inside the AG/rGO hybrid aeromaterial results in heat generation by means of the photothermal effect. Figure 2d displays the maximum front-

and backside temperature extracted from infrared (IR) images for different AG/rGO hybrid aeromaterials (cylindrical geometry, h = 10 mm and d = 12 mm) taken from the frontside (side that is illuminated with light) and backside (see Figure S4 for IR images). All aeromaterials were illuminated with a broadband light source (details in Materials and Methods) for only 1 s with an irradiance of 1.67 W cm^{-2}, in order to reduce the effect of heat conduction and accumulation. The short illumination time also demonstrates the rapid photothermal heating effect. Due to the negligible absorption properties of pristine AG, see UV−vis spectroscopy results in Figure 2e, no increase in temperature in the entire volume of the AG can be detected under illumination. In contrast to that, the pristine Aero-rGO heats up only at the illuminated front side, meaning that all light is directly absorbed in the surface region of the aeromaterial structure, confirming the light transmission measurements shown in Figure 2c. As can be seen in Figure 2d, the maximum frontside temperature increases with increasing volumetric rGO loading in the AG/rGO hybrid aeromaterials. UV−vis measurements confirm that the higher the volumetric rGO density, the higher the absorption over the whole wavelength spectrum (see Figure 2e, more details in SI Note 2), resulting in a higher frontside temperature as detected by thermography. In contrast, the backside temperature, as a measure for light penetration depth, reaches a maximum value of 66 °C for AG/rGO-47.3. For higher concentrations of rGO (94.7 μg cm^{-3}) the backside temperature decreases to 55 °C, whereas for pristine Aero-rGO no significant increase in temperature at the backside of the sample can be observed. This is highlighted as well in IR images (see Figure 2f) of the sample backside of AG/rGO-4.7, -94.7 and Aero-rGO with varying sample height (4−10 mm). The maximum temperature is extracted and is displayed in Figure 2g. For the hybrid aeromaterial transducers (AG/rGO-94.7 and -4.7) a heating effect in the entire volume can be detected, while for Aero-rGO the volumetric heating effect is already drastically reduced for 4 mm sample thickness. However, for AG/rGO-4.7 the volumetric heating effect is less pronounced, as the low rGO loading results in less absorption.

These results clearly demonstrate that an optimized volumetric rGO density in combination with a light-scattering material system can adjust the interaction volume of light within the AG/rGO hybrid aeromaterials, enabling a strong enhancement in volumetric light-to-heat conversion. The proposed concept of volumetric light-to-heat conversion is shown schematically in Figure 3, demonstrating the light−matter interaction for three different cases, namely pristine AG, Aero-rGO and AG/rGO with optimized volumetric loading of rGO. Light impinging on pristine AG is scattered multiple times within the structure, before leaving it again with only a negligible amount of light being absorbed, resulting in an isotropic light distribution, as shown in Figure 2a. The reason for multiple scattering events taking place can be found in the hierarchical microstructure, creating an optical disorder system with many Rayleigh scattering centers, as explained in more detail in Supporting Note 3. Thus, pristine AG is acting solely as a passive light diffuser and no light is converted into heat. In contrast, Aero-rGO (Figure 3b) absorbs all impinging light directly at the illumination side, resulting in strong localized heating of the microtubular structure. In contrast, AG/rGO with an optimized volumetric loading of rGO (Figure 3c) enables a combination of light scattering properties with the photothermal effect of the rGO flakes. Due to the
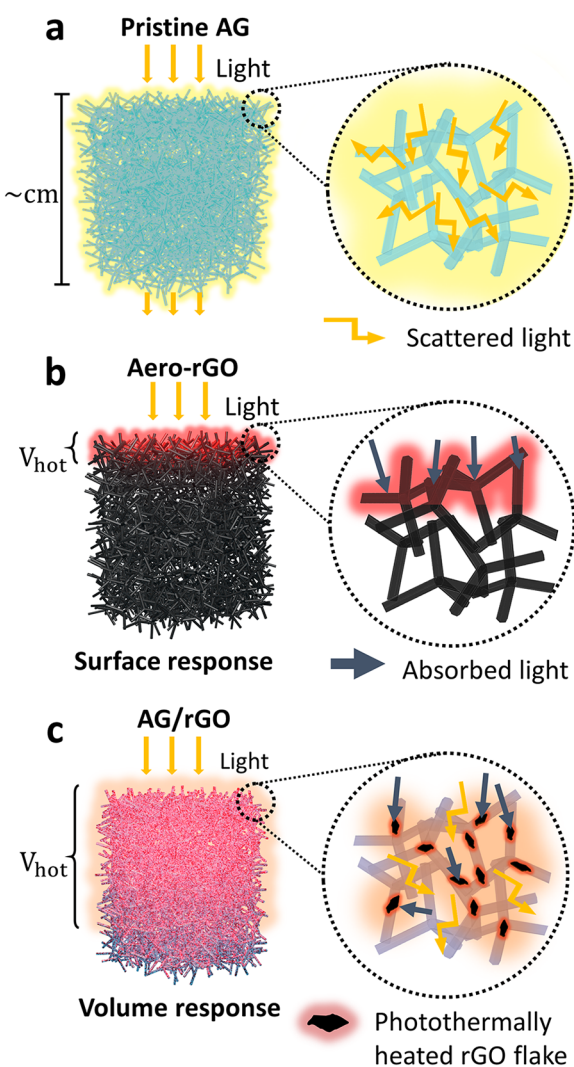
Figure 3. Schematic concept of proposed light−matter interaction in aeromaterials. Light scattering, associated light penetration, and light absorption resulting in diffferent photothermally active volumes for (a) pristine AG, (b) pristine Aero-rGO and (c) AG/rGO.

homogeneous distribution of rGO flakes in the AG framework structure, only a small amount of light is directly absorbed at the illumination side and most of the impinging light can penetrate deep into the structure by multiple scattering events before eventually impinging on a rGO flake, where light is absorbed and converted into heat by the photothermal effect. However, for too low volumetric loadings of rGO (e.g., 4.7 μg cm^{-3}) a noticeable amount of light can escape the aeromaterial structure without interacting with the photothermal nanomaterial. Therefore, an optimized volumetric density of rGO inside the AG is necessary to balance between light scattering, transmission, and absorbance.

Activation of Gas Volume. The enhanced volumetric light absorption in combination with the extremely low volumetric heat capacity ($\sim$2.5 kJ m^{-3} K^{-1}) (Calculation details in SI Note 4) and high gravimetric surface area ($\sim$74.153 m^2 g^{-1}) (Calculation details in SI Note 5) of the here developed nano- and microengineered transducer material enables a rapid and repeatable activation (heating) of
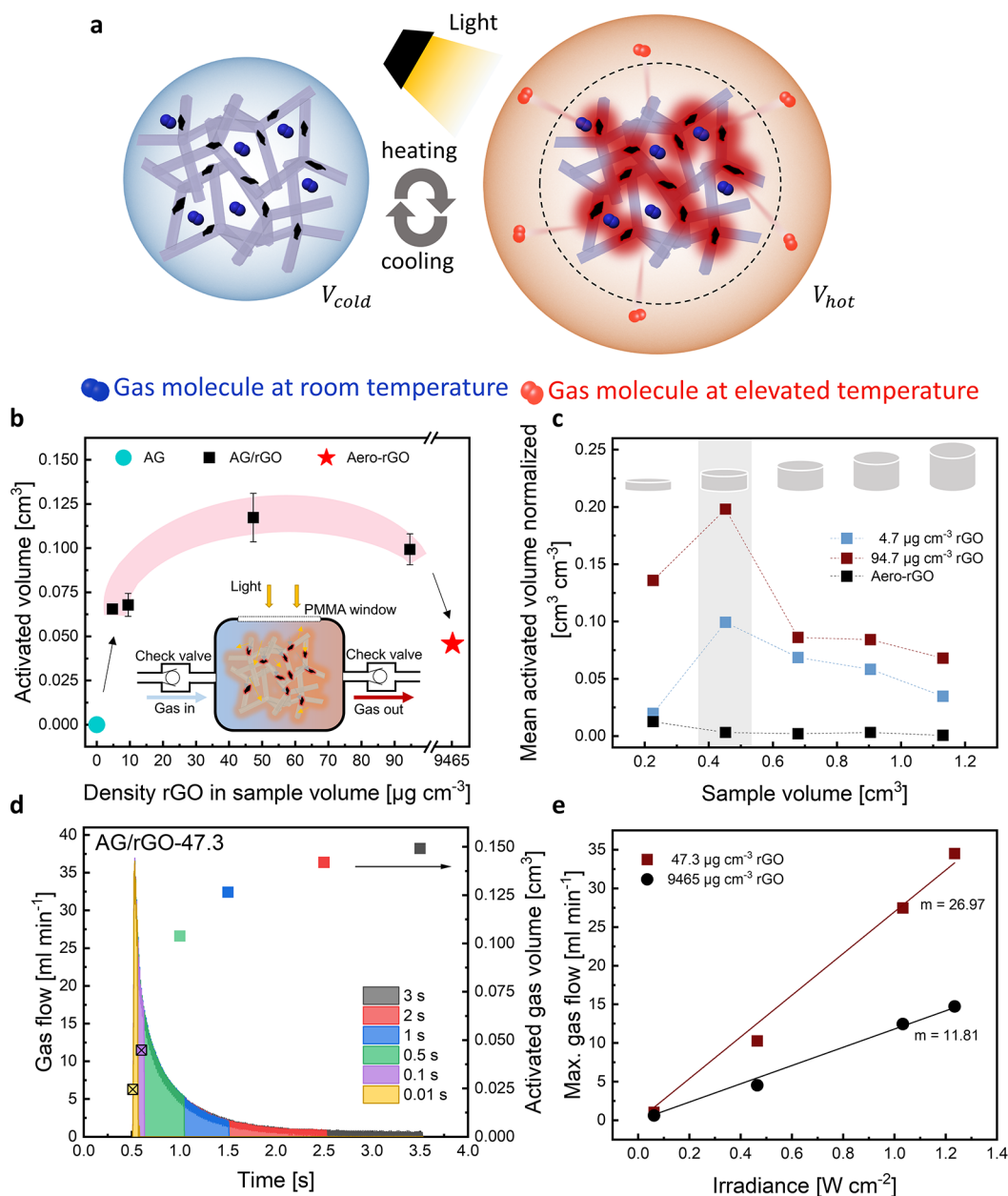
Figure 4. Characterization of volumetric gas activation. (a) Schematic of gas activation in AG/rGO hybrid aeromaterial. (b) Mean activated gas volume for 1 pulse (1 s) for pristine AG, AG/rGO with different volumetric loadings of rGO and pristine Aero-rGO. The inset shows a schematic of the measurement setup. (c) Mean activated volume normalized to sample volume measured for different sample heights of AG/rGO with low and high loadings of rGO as well as for Aero-rGO. (d) Gas flow induced by gas activation versus time for different pulse lengths with calculated activated gas volume on the second axis for a AG/rGO-47.3 sample. (e) Maximum detected gas flow versus irradiance for AG/rGO-47.3 and Aero-rGO.

macroscopic gas volumes, as schematically shown in Figure 4a. Based on the low volumetric heat capacity, the temperature of the AG/rGO hybrid aeromaterial rapidly increases when illuminated with light; i.e., in only 1 s, the temperature increases to around 300 °C (for AG/rGO-94.7). The heat generated by the photothermal effect within the aeromaterial structure is transferred to the gas phase within milliseconds by utilizing its high surface area. Under isobaric conditions, this causes a rapid volume expansion of the gas within the aeromaterial, according to the ideal gas law. Simultaneously, the open porous framework structure (porosity >99.9%) with

micrometer-sized voids, allows rapid gas exchange out of and into the aeromaterial structure. Without illumination, the structure cools down immediately, and the process can be repeated. A similar effect has been reported before, based on the Joule-heating of framework structures of graphene;[23] however, electrical contacts are required, whereas here, we present wireless activation of macroscopic gas volumes using light.

In order to further quantify the volumetric light-to-heat conversion and related rapid gas activation of our hybrid aeromaterial transducer as a function of volumetric rGO

loading, illumination time, and irradiance, AG/rGO hybrid aeromaterials were placed in an airtight chamber equipped with two check valves, as shown in the inset of Figure 4b, and in Figure S5 and Figure S6. In this configuration, the illumination of an AG/rGO hybrid aeromaterial through a poly(methyl methacrylate) window results in a rapid temperature increase of the gas within the sample volume, causing a volume expansion. The extent of the volume expansion, according to the ideal gas law, thereby depends on the temperature and the amount of activated gas and thus on the properties of the transducer material. The check valves allow directional gas flow through a connected glass tube containing 1 mL of dyed water. By applying a light pulse, the water droplet is pushed through the glass tube (see Supplementary Video 1), with the distance being a direct measure of the activated gas volume.

The mean activated gas volume for one light pulse of 1 s for different volumetric rGO loadings is displayed in Figure 4b (irradiance of 1.24 W cm^{-2}, f = 0.5 Hz, more details see Materials and Methods). In accordance with the results presented in Figure 2, there is no gas activated in the case of pristine AG, as only negligible light absorption occurs. With an increasing volumetric loading of rGO, the activated gas volume increases to a maximum value of 0.11 cm^3 for AG/rGO-47.3, which is around 9.7% of the total volume of the aeromaterial structure. Compared to pristine Aero-rGO, this means an improvement by a factor of 2.44 in terms of volumetric gas activation, as for Aero-rGO, a gas volume of only around 0.045 cm^3 is activated.

Figure 4c shows the mean volume of activated gas normalized to the total volume of the hybrid aeromaterial for cylindrical sample geometries with varying height (2−10 mm) for the highest (AG/rGO-94.7) and lowest rGO loading (AG/rGO-4.7) (see Figure S7), as well as for pristine Aero-rGO. The highest gas activation for 1 s illumination time is reached by AG/rGO-94.7 with a height of 4 mm. Around ∼20% of the total aeromaterial volume is activated, which is by a factor of 66 higher compared to pristine Aero-rGO. The normalized activated gas volume decreases with further increasing height for both AG/rGO-94.7 and AG/rGO-4.7. In contrast, pristine Aero-rGO shows an almost constant value of ∼0.3% of volumetric gas activation irrespective of height. This significantly indicates that the amount of activated gas for pristine Aero-rGO is solely attributed to the mentioned surface effect (see also Figure S8). As an approximation, an ideal flat 2D surface with a radius of 6 mm provides a surface area of 1.13 cm^2 that can be used for gas activation by the photothermal effect, whereas a cylindrical hybrid aeromaterial, e.g., AG/rGO-94.7, with a radius of 6 mm and height of 4 mm, provides a total surface area of ∼500 cm^2 (details on the calculation can be found in SI Note 6). Assuming that the entire volume of the aeromaterial transducer is used for gas activation, the available surface area is by a factor of ∼445 larger, enabling the rapid activation of larger gas volumes. Note that due to the low density of gases, only the gas volume which is in close proximity to a heated surface can be rapidly activated.

Figure 4d displays the gas flow generated by an AG/rGO-47.3 hybrid aeromaterial (d = 12 mm and h = 10 mm), which was illuminated with single light pulses as a function of pulse widths (0.01 to 3 s) at a constant irradiance of 1.24 W cm^{-2} (Figure S9 for AG/rGO-94.7). The gas flow directly peaks after only 22 ms of illumination with a maximum flow of ∼36 mL min^{-1}, before decreasing exponentially. The maximum detected gas flow for all pulse lengths was 36 mL min^{-1} and the shape of the curve is the same for all applied pulse widths, while the gas flow drops to zero immediately after illumination is turned off. As shown in Figure 4d, the activated gas volume increases with increasing pulse width. However, a maximum value for long pulse lengths (1−3 s) of roughly 0.15 cm^3 is approached, as a mean temperature is reached and hence no further gas activation occurs.

Figure 4e shows the influence of the light intensity on the maximum gas flow for Aero-rGO and AG/rGO-47.3 for a pulse length of 1 s. The maximum gas flow, as indirect measure for the activated gas volume, increases linearly with light intensity for both systems, as a higher light intensity results in higher temperatures generated by the photothermal effect and hence, more gas is activated. However, the slope for AG/rGO-47.3 (26.97 mL cm^2 min^{-1} W^{-1}) is more than twice as steep as for Aero-rGO (11.8 mL cm^2 min^{-1} W^{-1}). While for Aero-rGO all light is absorbed close to the illumination side, an increase in light intensity only increases the surface temperature, which in return does only lead to a marginal change in activated gas volume. However, for the AG/rGO hybrid aeromaterial, higher light intensities also result in deeper light penetration, thereby resulting in a stronger increase of activated gas with increasing light intensity compared with pristine Aero-rGO.

Optimizing the volumetric light-to-heat conversion in AG/rGO hybrid aeromaterials requires the balance between light scattering, transmission, and absorbance of light by photothermal material. The results indicate the importance to create a homogeneous heating effect in the entire volume rather than heating only parts of the structure to high temperatures in order to achieve the highest values for gas activation within the structure. For the here shown volumetric loadings of rGO, AG/rGO-47.3 showed the best performance in terms of a volumetric heating effect and gas activation, as the highest values for flow rate (36 mL min^{-1}) and activated gas volume (∼0.15 cm^3) were measured, matching the results of the temperature measurement, where the highest backside temperature was measured for AG/rGO-47.3, and hence, indicating that light can interact with photothermal agents in a large part of the structure.

Applications. The observed enhancement in volumetric light−matter interaction provided by our optimized photothermal aeromaterial transducer enables manifold wireless applications that make use of the rapidly activated gas volumes at high repetition rates. We here present proof-of-concept demonstrators for untethered, light-driven, and light-controlled pneumatic soft actuators and wireless light-powered microfluidic pumps. Conventional soft actuators for soft robotic applications are based on pneumatic actuation systems that require pressurized air to create movements, which is usually delivered via air hoses.[31,32] This tethered connection strongly limits the autonomy, range of movement and the operational flexibility of soft robots.[31,32] While approaches to enable autonomous soft robotic system often rely on bulky carry-on systems,[31,33] e.g., gas storage tanks,[34,35] battery packs[31] or chemical reaction chambers,[32] that increase weight and thus limit the operational time,[33−35] we here demonstrate an autonomous untethered soft and lightweight pneumatic actuator that is purely powered and controlled by light. The proof-of-concept demonstrators presented here are operated using the best performing sample type AG/rGO-47.3.
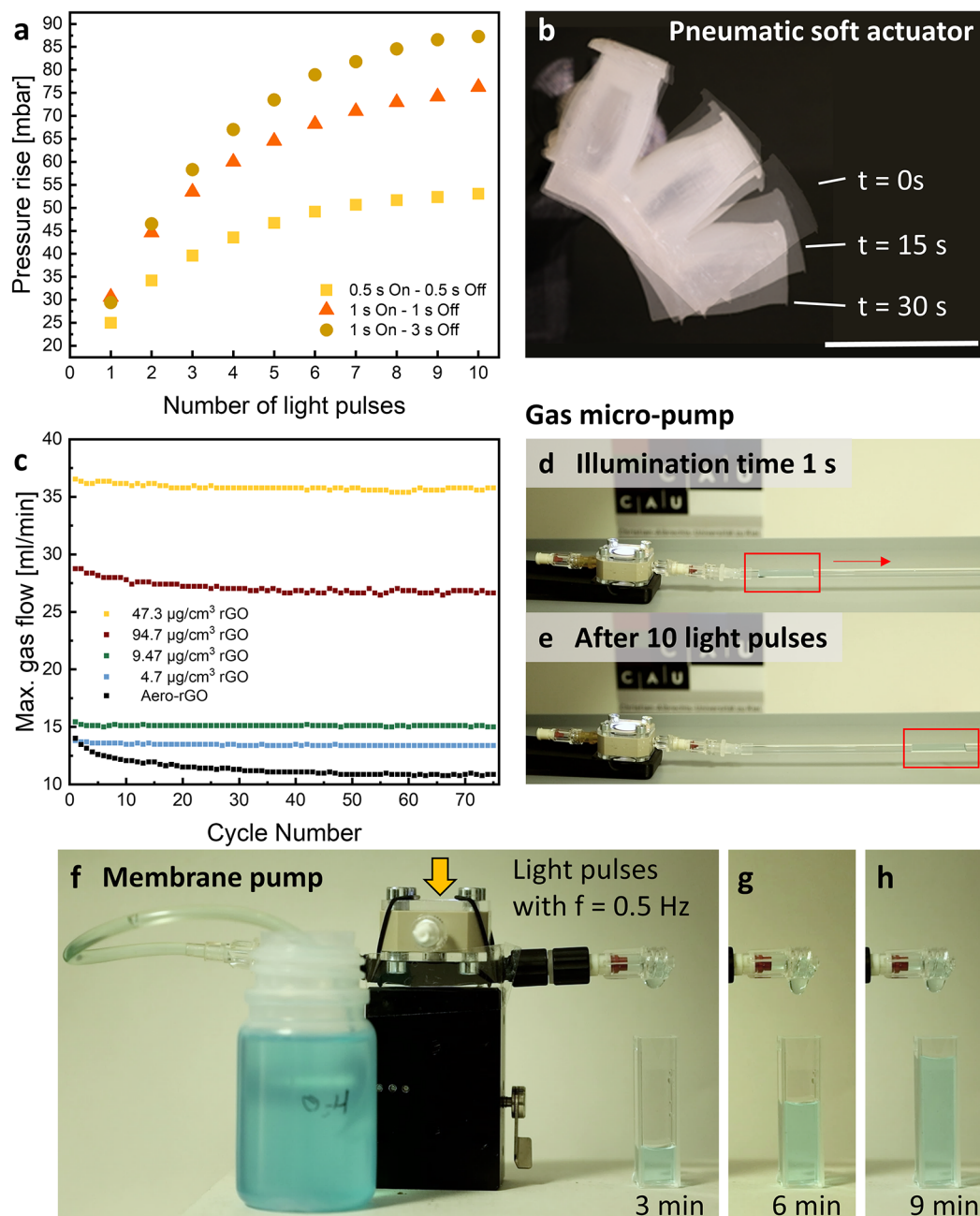
Figure 5. Application scenarios for micro- and nanoengineered AG/rGO hybrid aeromaterials. (a) Pressure rise generated by an AG/rGO-47.3 sample in an external pressure chamber versus number of applied light pulses for different illumination frequencies. (b) Merged photograph of free-standing (untethered) soft pneumatic actuator powered by light at three different time points of actuation. (c) Maximum detected gas flow versus cycle number for cyclic illumination with 0.5 Hz and an irradiance of 1.24 W cm^{-2}. (d,e) Photograph of micropump pushing a droplet of dyed water through a glass tube, showing the covered distance after 10 light pulses. (f−h) Sequence of images of a wireless light-powered membrane pump in operation after 3, 6, and 9 min.

The concept is based on the encapsulation of the photothermal aeromaterial transducer in a closed chamber that is directly connected to a conventional soft pneumatic actuator by using a check valve (see Figure S10). Illuminating the transducer material with light results in an increase in pressure in a closed system. Figure 5a shows the pressure rise measured for AG/rGO-47.3 as a function of light pulses for three different illumination frequencies and pulse-widths. As can be seen in Figure 5a, the pressure can be adjusted by the number of light pulses. A maximum increase in pressure of

~87 mbar is reached in ~40s, corresponding to 10 light pulses (illumination time of 1 s with a recovery time of 3 s). Thereby, a pneumatic soft actuator can be deformed and controlled by light, as shown in Figure 5b. Each light pulse creates an increase in pressure, bending the soft robotic arm in a steplike motion until saturation pressure is reached. Mounting the pneumatic soft actuator directly to the chamber without any check valves even allows the soft pneumatic actuator to bend and relax with only one single light pulse in a reversible manner (see Supplementary Video 2).

Next to applications in soft robotics, the aeromaterial transducer can be utilized for wireless, light-powered, and light-controlled fluidic (gas and liquid) micropumps. Figure 5c shows the maximum gas flow over 77 light pulses (pulse width of 1 s at a frequency of 0.5 Hz and an irradiance of 1.24 W cm^{-2}) for AG/rGO aeromaterial transducers with different volumetric rGO loadings as well as for pristine Aero-rGO. AG/rGO-47.3 shows the highest measured gas flow rate of ~36 mL min^{-1}, which is by more than 33% higher compared to the pristine Aero-rGO. Furthermore, while all AG/rGO hybrid aeromaterials show an almost constant gas flow over the entire cycle range, the gas flow for Aero-rGO decreases slowly from ~14 mL min^{-1} until a constant value of ~10.8 mL min^{-1} is reached after roughly 45 cycles. We suspect that the decrease is associated with a heat accumulation at the illuminated surface. Thereby the difference in temperature (T_{light_on} vs T_{light_off}) decreases over time, resulting a lower volume expansion until an equilibrium state is reached.

The pumped fluidic volume can be easily controlled by varying pulse lengths and applied light frequencies, as demonstrated in Figure 5d, e, showing a light driven micropump with a pump rate of ~3.51 mL min^{-1} pushing a droplet of dyed water through a glass tube (see Supplementary Video 1). Furthermore, a wireless light-powered and light-controlled membrane pump could be realized (see Figure 5f–h and Supplementary Video 3), utilizing the rapid switching in pressure to repeatable strain a flexible membrane in order to pump a liquid (details on the setup can be found in Figure S11), achieving a pump rate of ~0.44 mL min^{-1} without optimization.

It should be noted that for all the application scenarios suggested here, the lightweight nature of the hybrid aeromaterials makes them extremely resistant to vibrations and forces, e.g., caused by high accelerations, ensuring that no structural damage occurs over time, especially when encapsulated.

CONCLUSION

In conclusion, we here show an advanced fabrication concept for the controlled combination of different nanomaterials and their functionalities in a hybrid 3D assembly, thereby overcoming the limitations of their pristine variants. We demonstrate a hybrid SiO_2/rGO photothermal aeromaterial transducer that enables an ultrarapid and enhanced volumetric photothermal response by a factor of 2.44 compared to the pristine carbon nanomaterial-based variant. By combining the light scattering properties of a highly porous SiO_2 framework structure with the photothermal properties of rGO, we are able to tailor the light−matter interaction volume in a controlled manner by adjusting the volumetric density of rGO nanoflakes within the hybrid aeromaterial. Utilizing the enhanced photothermal interaction volume in combination with the high surface area and low volumetric heat capacity of the porous transducer material allows for ultrarapid activation of macroscopic gas volumes, enabling multiple functionalities and application scenarios based on the conversion of light into heat. While we here demonstrate proof-of-concept demonstrators for untethered, light-driven, and light-controlled pneumatic soft actuators and wireless light-powered microfluidic pumps, the hybrid aeromaterials could be used to generate a directional pressure wave, e.g., for light-controlled, directional motion. In perspective, a directional and also dynamic illumination of different sections of an extended hybrid aeromaterial could generate several pressure waves emanating from parts of the material, which result in a certain direction of propagation through destructive and constructive interference. By controlling the frequency and changing the order of illumination, the resulting pressure wave could be shaped in relatively arbitrarily manner. Next to that, the concept could be used for advances in the fields of environmental remediation, such as the synthesis of solar fuels by gas phase (photo)catalysis, solar thermal heating and desalination, as well as photoacoustics. For example, it is conceivable to use the photothermal transducer material for photocatalysis applications to simultaneously pump gas and trigger a chemical reaction by temperature activation. Expanding the concept to fabricate lightweight hybrid aeromaterial transducers by utilizing the extraordinary properties of other 1D and 2D nanomaterials, including quantum dots, MXenes and catalysts, allows functionalities well-beyond that of photothermal conversion.

MATERIALS AND METHODS

Materials. Polyvinyl butyral, zinc (grain size 1−5 μm), ethanol, TEOS, ammonia hydroxide solution, graphene oxide dispersion, and L-ascorbic acid.

Graphene oxide (GO) was obtained by procedures reported elsewhere.[36,37] Dispersion were prepared by tip sonication in water.

Aeroglass (AG) structures were fabricated using tetrapodal ZnO (t-ZnO) as sacrificial template for a wet chemical coating process with SiO_2 based on the Stoeber synthesis.[38,39] The fabrication of sacrificial templates is described elsewhere.[22,40,41] Briefly, t-ZnO was produced via a flame transport synthesis,[41,42] pressed into desired shape using a metal mold, and subsequently sintered in an oven (1150 °C for 5 h) to create an interconnected network of ZnO tetrapods. The wet chemical approach for coating the ZnO network with a thin layer of SiO_2 is based on the Stoeber process. In detail, two solutions with different ratios of ethanol, tetraethylorthosilicate (TEOS) and ammonia hydroxide solution (25%), namely, V1 (ratio 10:0.1:3) and V2 (ratio 10:0.05:3) were used in this work. The silica solution was prepared by mixing ethanol and TEOS, followed by the addition of an ammonia hydroxide solution. The sacrificial ZnO templates were immersed in the silica solution for 45 min during which the solution turned turbid and the entire ZnO template was coated with a thin layer of amorphous SiO_2. The coating was performed in a two-step process: first a coating with ratio V1 was applied, followed by rinsing in ethanol and drying on a Teflon plate, before the second coating was applied using ratio V2. Samples were stored in distilled water for 24 h, followed by wet chemical removal of the sacrificial ZnO template with 1 M hydrochloric acid. To remove residuals, the samples were washed thoroughly with water before being transferred into pristine ethanol for critical point drying (Leica EM CPD300).

Functionalization of Aeroglass. Prior to the two-step silica coating step, the ZnO templates were infiltrated with a water-based dispersion of nanomaterial, as described elsewhere.[22,40] This led to partial coating of the nanomaterial on the ZnO tetrapod arms. To control the amount of nanomaterial within the aeroglass structure, the concentration of the nanomaterial dispersion was adjusted. For functionalization with reduced graphene oxide, the ZnO templates were coated with graphene oxide flakes which were reduced in an additional step after the wet chemical removal of ZnO using diluted L-ascorbic acid (24 h, 50 °C). The rGO functionalized aeroglass is named AG/rGO.

Aero-rGO samples were fabricated by drop infiltrating sacrificial t-ZnO templates with graphene oxide dispersion and subsequent drying, resulting in a homogeneous coating of the tetrapod arms with graphene oxide flakes, as described elsewhere in more detail.[22] The infiltration step was repeated six times. Diluted L-ascorbic acid (24 h, 50 °C) was used to reduce graphene oxide, followed by wet chemical

removal of ZnO, washing, and drying, as described for the fabrication of aeroglass.

SEM measurements were performed using a Zeiss Supra 55VP.

TEM was carried out using an FEI Tecnai F-30 G2 Stwin operated at 300 kV. The microscope is equipped with an EDAX Si/Li detector for elemental analysis and a Gatan Tridiem 863P post column image filter (GIF) allowing for electron energy loss spectroscopy (EELS) measurements. AG and AG/rGO specimens were prepared for TEM investigation by grinding a small amount of material in butanol followed by drop coating onto lacey carbon coated Cu TEM grids.

UV−vis spectroscopy was carried out in water to avoid measurement artifacts due to light scattering of the samples. A sample thickness of 2 mm was chosen to ensure a transmitting beam through the sample. A customized photometer (light source HL-2000-FHSA-LL by Ocean Insight, Ostfildern, Germany and spectrometer Flame-S-VIS-NIR_ES by Ocean Insight, Ostfildern, Germany), controlled by a customized LabVIEW program (National Instruments, Austin, TX, USA, version 2012) was used for the measurement and the data was evaluated using Matlab (The MathWorks Inc., Natick, MA, USA, version R2021a).

Raman measurements were conducted by using an alpha300 RA (WITec) microscope with a triple grating spectrometer (600 g mm^{-1}) and a charge-coupled device detector. The excitation wavelength of the laser was 532.2 nm with a laser spot size on the sample of ∼1.41 μm and a maximum power of 52 mW.

Light source for illuminating the samples with white light was a beamer (Acer, DLP Projector, DNX0906) in combination with an overhead projector lens to focus the beamer light to a spot size of 12 mm. A spectrum was recorded with an Ocean Optics spectrometer FLAME-S-XR1-ES (200−1025 nm), see Figure S12. For controlling the illumination time, as well as the light power, a power point presentation with preset display times and varying grayscale of displayed images was used.

Thermography was performed placing the samples directly in the focus point of the light source, and temperature was recorded with an IR camera (InfraTec, PIR uc 180) from three different directions. In more detail, the temperature of the sample frontside (illumination side) and the sample backside were recorded as well as the side view to gain information about the temperature gradient within the sample. The samples were cylindrical shaped with a diameter of 12 mm, height of 4 mm to 10 mm and a conical shaped taphole on the illumination side of the sample (only for comparison of different graphene loadings). The samples were illuminated for 1 s with an irradiance of 1.67 W cm^{-2}, and the image with the maximum temperature was selected. The irradiance was measured with a power meter (Thorlabs Photometer, S425C-L with Interface PM100USB and Thorlabs Opitcal Power Monitor).

Measurements on volumetric gas activation were conducted using the same setup as for thermography, but placing the samples in an enclosed chamber with a poly(methyl methacrylate) window on the illumination side and two check valves (see Figure S5 and Figure S6), from which one was connected to a glass tube which contained 1 mL of dyed water. The samples were illuminated with a frequency of 0.5 Hz and an irradiance of 1.24 W cm^{-2}. In total, 10 light pulses were performed for each sample. The activated gas volume was calculated from the distance the water droplet was pushed through the glass tube and the diameter of the tube and averaged over 10 light pulses. The activated gas volume for varying sample heights was measured with spacers to ensure an equal distance to the light source as well as no free volume above the illumination side.

Flow measurements were conducted using an enclosed chamber equipped with two check valves and a flow sensor (Honeywell AWM3100 V). Samples have been illuminated with an irradiance of 1.24 W cm^{-2} and pulse widths ranging from 0.01 up to 3 s. The activated gas volume was calculated by integration of the measurement data.

Light transmission was measured with a power meter (Thorlabs Photometer, S425C-L with Interface PM100USB and Thorlabs Opitcal Power Monitor) placed directly behind the sample which was illuminated with an irradiance of 1.24 W cm^{-2} for 3 s.

Pressure measurements were conducted using a pressure sensor (Kistler, 4260A) mounted on an empty chamber, which was connected via a check valve to the enclosed chamber containing the sample as described before.

ASSOCIATED CONTENT

Data Availability Statement

The data that support the findings of this study are available from the corresponding authors upon request.

ⓈⒾ Supporting Information

The Supporting Information is available free of charge at https://pubs.acs.org/doi/10.1021/acsnano.3c05329.

> Photograph of functionalized aeroglass samples, additional SEM images, TEM diffraction pattern of aeroglass, additional infrared images of hybrid aeroglass, schematic and photograph of airtight sample chamber, photograph of hybrid aeroglass samples, additional measurements on gas activation to demonstrate the surface effect for pristine Aero-rGO samples, gas flow measurement for AG/rGO-94.7, photograph of setup for untethered soft pneumatic actuator, schematic concept of wireless light-powered membrane pump, spectrum of beamer, details on TEM investigation of aeroglass, comment on UV−vis spectroscopy, details on light scattering in aeroglass, calculation of volumetric specific heat capacity and specific surface area (PDF)
>
> Supplementary Video 1: gas pump (AVI)
> Supplementary Video 2: soft actuator (AVI)
> Supplementary Video 3: membrane pump (AVI)

AUTHOR INFORMATION

Corresponding Author

Fabian Schütt − *Functional Nanomaterials, Kiel University, 24143 Kiel, Germany; Kiel Nano, Surface and Interface Science KiNSIS, Kiel University, 24118 Kiel, Germany*; Email: fas@tf.uni-kiel.de

Authors

Lena M. Saure − *Functional Nanomaterials, Kiel University, 24143 Kiel, Germany*

Niklas Kohlmann − *Synthesis and Real Structure, Department for Materials Science, Kiel University, 24143 Kiel, Germany*; orcid.org/0000-0001-8494-118X

Haoyi Qiu − *Functional Nanomaterials, Kiel University, 24143 Kiel, Germany*; orcid.org/0000-0003-2379-3333

Shwetha Shetty − *Materials Research Centre, Indian Institute of Science, Bangalore, Karnataka 560012, India*

Ali Shaygan Nia − *Department of Chemistry and Food Chemistry, Center for Advancing Electronics Dresden (cfaed), Dresden University of Technology, 01062 Dresden, Germany*

Narayanan Ravishankar − *Materials Research Centre, Indian Institute of Science, Bangalore, Karnataka 560012, India*; orcid.org/0000-0003-0012-046X

Xinliang Feng − *Department of Chemistry and Food Chemistry, Center for Advancing Electronics Dresden (cfaed), Dresden University of Technology, 01062 Dresden, Germany*

Alexander Szameit − *Department for Physics and Department of Life, Light & Matter, University of Rostock, 18059 Rostock, Germany*

Lorenz Kienle − *Synthesis and Real Structure, Department for Materials Science, Kiel University, 24143 Kiel, Germany; Kiel Nano, Surface and Interface Science KiNSIS, Kiel University, 24118 Kiel, Germany*

Rainer Adelung − *Functional Nanomaterials, Kiel University, 24143 Kiel, Germany; Kiel Nano, Surface and Interface Science KiNSIS, Kiel University, 24118 Kiel, Germany;* ⊙ orcid.org/0000-0002-2617-678X

Author Contributions

L.M.S., F.S., S.S. and R.A. developed the hybrid AG/rGO aeromaterials and designed the study. A.S.N. prepared the GO dispersion. L.M.S. fabricated the samples, carried out the experiments and evaluated the data. H.Q. performed Raman measurements. N.K. and L.K. performed TEM measurements and evaluated the TEM specific data. L.M.S., F.S. and R.A. finalized the study and wrote the paper. All of the authors have contributed to the discussion of the results and reviewed the manuscript.

Notes

The authors declare no competing financial interest.

This work has been published on a preprint server: Lena M. Saure, Niklas Kohlmann, Haoyi Qiu, Shwetha Shetty, Ali Shaygan Nia, Narayanan Ravishankar, Xinliang Feng, Alexander Szameit, Lorenz Kienle, Rainer Adelung, Fabian Schütt*; Hybrid aeromaterials for enhanced and rapid volumetric photothermal response. 2023, arXiv. DOI:10.48550/arXiv.2303.14014 (accessed Sept. 28, 2023)

REFERENCES

(1) Gao, M.; Zhu, L.; Peh, C. K.; Ho, G. W. Solar absorber material and system designs for photothermal water vaporization towards clean water and energy production. *Energy Environ. Sci.* **2019**, *12* (3), 841−864.

(2) Elbrashy, A.; Aboutaleb, F.; El-Fakharany, M.; Essa, F. A. Experimental study of solar air heater performance with evacuated tubes connected in series and involving nano-copper oxide/paraffin wax as thermal storage enhancer. *Environmental science and pollution research international* **2023**, *30*, 4603.

(3) Yin, Y.; Chen, H.; Zhao, X.; Yu, W.; Su, H.; Chen, Y.; Lin, P. Solar-absorbing energy storage materials demonstrating superior solar-thermal conversion and solar-persistent luminescence conversion towards building thermal management and passive illumination. *Energy Conversion and Management* **2022**, *266*, 115804.

(4) Ravi Kumar, K.; Krishna Chaitanya, N.; Sendhil Kumar, N. Solar thermal energy technologies and its applications for process heating and power generation - A review. *Journal of Cleaner Production* **2021**, *282*, 125296.

(5) Tschopp, D.; Tian, Z.; Berberich, M.; Fan, J.; Perers, B.; Furbo, S. Large-scale solar thermal systems in leading countries: A review and comparative study of Denmark, China, Germany and Austria. *Applied Energy* **2020**, *270*, 114997.

(6) Yoon, T. P.; Ischay, M. A.; Du, J. Visible light photocatalysis as a greener approach to photochemical synthesis. *Nature Chem.* **2010**, *2* (7), 527−532.

(7) Banerjee, S.; Pillai, S. C.; Falaras, P.; O'Shea, K. E.; Byrne, J. A.; Dionysiou, D. D. New Insights into the Mechanism of Visible Light Photocatalysis. *journal of physical chemistry letters* **2014**, *5* (15), 2543−2554.

(8) Ahmed, S.; Khan, F. S. A.; Mubarak, N. M.; Khalid, M.; Tan, Y. H.; Mazari, S. A.; Karri, R. R.; Abdullah, E. C. Emerging pollutants and their removal using visible-light responsive photocatalysis - A comprehensive review. *Journal of Environmental Chemical Engineering* **2021**, *9* (6), 106643.

(9) Dash, B. S.; Jose, G.; Lu, Y.-J.; Chen, J.-P. Functionalized Reduced Graphene Oxide as a Versatile Tool for Cancer Therapy. *International journal of molecular sciences* **2021**, *22* (6), 2989.

(10) Tee, S. Y.; Win, K. Y.; Goh, S. S.; Teng, C. P.; Tang, K. Y.; Regulacio, M. D.; Li, Z.; Ye, E. Chapter 1. Introduction to Photothermal Nanomaterials. In *Photothermal Nanomaterials*; Ye, E., Li, Z., Eds.; Nanoscience & Nanotechnology Series; Royal Society of Chemistry, 2022; pp 1−32. DOI: 10.1039/9781839165177-00001.

(11) Chen, H.; Wu, S.-L.; Wang, H.-L.; Wu, Q.-Y.; Yang, H.-C. Photothermal Devices for Sustainable Uses Beyond Desalination. *Adv. Energy Sustain Res.* **2021**, *2* (3), 2000056.

(12) Ito, Y.; Tanabe, Y.; Han, J.; Fujita, T.; Tanigaki, K.; Chen, M. Multifunctional Porous Graphene for High-Efficiency Steam Generation by Heat Localization. *Advanced materials (Deerfield Beach, Fla.)* **2015**, *27* (29), 4302−4307.

(13) Ren, H.; Tang, M.; Guan, B.; Wang, K.; Yang, J.; Wang, F.; Wang, M.; Shan, J.; Chen, Z.; Wei, D.; Peng, H.; Liu, Z. Hierarchical Graphene Foam for Efficient Omnidirectional Solar-Thermal Energy Conversion. *Advanced materials (Deerfield Beach, Fla.)* **2017**, *29* (38), 1702590.

(14) Li, R.; Zhang, L.; Shi, L.; Wang, P. MXene Ti3C2: An Effective 2D Light-to-Heat Conversion Material. *ACS Nano* **2017**, *11* (4), 3752−3759.

(15) Zou, Y.; Zhang, Y.; Yu, Q.; Chen, H. Photothermal bactericidal surfaces: killing bacteria using light instead of biocides. *Biomaterials science* **2021**, *9* (1), 10−22.

(16) Yang, F.; Zhang, Y.; Yang, X.; Zhong, M.; Yi, Z.; Liu, X.; Kang, X.; Luo, J.; Li, J.; Wang, C.-Y.; Zhao, H.-B.; Fu, Z.-B.; Tang, Y.-J. Enhanced Photothermal Effect in Ultralow-Density Carbon Aerogels with Microporous Structures for Facile Optical Ignition Applications. *ACS Appl. Mater. Interfaces* **2019**, *11* (7), 7250−7260.

(17) Jiang, Q.; Tian, L.; Liu, K.-K.; Tadepalli, S.; Raliya, R.; Biswas, P.; Naik, R. R.; Singamaneni, S. Bilayered Biofoam for Highly Efficient Solar Steam Generation. *Advanced materials (Deerfield Beach, Fla.)* **2016**, *28* (42), 9400−9407.

(18) Nicola, F. de; Tenuzzo, L. D.; Viola, I.; Zhang, R.; Zhu, H.; Marcelli, A.; Lupi, S. Ultimate Photo-Thermo-Acoustic Efficiency of Graphene Aerogels. *Sci. Rep.* **2019**, *9* (1), 13386.

(19) Gao, M.; Peh, C. K.; Zhu, L.; Yilmaz, G.; Ho, G. W. Photothermal Catalytic Gel Featuring Spectral and Thermal Management for Parallel Freshwater and Hydrogen Production. *Adv. Energy Mater.* **2020**, *10* (23), 2000925.

(20) Li, Y.; Chang, H.; Wang, Z.; Shen, Q.; Liu, X.; Xue, J.; Jia, H. A 3D C@TiO2 multishell nanoframe for simultaneous photothermal catalytic hydrogen generation and organic pollutant degradation. *J. Colloid Interface Sci.* **2022**, *609*, 535−546.

(21) Geng, H.; Zhou, K.; Zhou, J.; Ma, H.; Lv, C.; Li, C.; Xu, Z.; Qu, L. Sunlight-Driven Water Transport via a Reconfigurable Pump. *Angewandte Chemie (International ed. in English)* **2018**, *57* (47), 15435−15440.

(22) Rasch, F.; Schütt, F.; Saure, L. M.; Kaps, S.; Strobel, J.; Polonskyi, O.; Nia, A. S.; Lohe, M. R.; Mishra, Y. K.; Faupel, F.; Kienle, L.; Feng, X.; Adelung, R. Wet-Chemical Assembly of 2D Nanomaterials into Lightweight, Microtube-Shaped, and Macroscopic 3D Networks. *ACS Appl. Mater. Interfaces* **2019**, *11* (47), 44652−44663.

(23) Schütt, F.; Rasch, F.; Deka, N.; Reimers, A.; Saure, L. M.; Kaps, S.; Rank, J.; Carstensen, J.; Kumar Mishra, Y.; Misseroni, D.; Romani Vázquez, A.; Lohe, M. R.; Shaygan Nia, A.; Pugno, N. M.; Feng, X.; Adelung, R. Electrically powered repeatable air explosions using microtubular graphene assemblies. *Mater. Today* **2021**, *48*, 7−17.

(24) Schütt, F.; Zapf, M.; Signetti, S.; Strobel, J.; Krüger, H.; Röder, R.; Carstensen, J.; Wolff, N.; Marx, J.; Carey, T.; Schweichel, M.; Terasa, M.-I.; Siebert, L.; Hong, H.-K.; Kaps, S.; Fiedler, B.; Mishra,

Y. K.; Lee, Z.; Pugno, N. M.; Kienle, L.; Ferrari, A. C.; Torrisi, F.; Ronning, C.; Adelung, R. Conversionless efficient and broadband laser light diffusers for high brightness illumination applications. *Nat. Commun.* **2020**, *11* (1), 1437.

(25) Yang, D.; Velamakanni, A.; Bozoklu, G.; Park, S.; Stoller, M.; Piner, R. D.; Stankovich, S.; Jung, I.; Field, D. A.; Ventrice, C. A.; Ruoff, R. S. Chemical analysis of graphene oxide films after heat and chemical treatments by X-ray photoelectron and Micro-Raman spectroscopy. *Carbon* **2009**, *47* (1), 145−152.

(26) Paredes, J. I.; Villar-Rodil, S.; Solís-Fernández, P.; Martínez-Alonso, A.; Tascón, J. M. D. Atomic force and scanning tunneling microscopy imaging of graphene nanosheets derived from graphite oxide. *Langmuir: the ACS journal of surfaces and colloids* **2009**, *25* (10), 5957−5968.

(27) Moon, I. K.; Lee, J.; Ruoff, R. S.; Lee, H. Reduced graphene oxide by chemical graphitization. *Nat. Commun.* **2010**, *1*, 73.

(28) Chen, W.; Yan, L.; Bangal, P. R. Preparation of graphene by the rapid and mild thermal reduction of graphene oxide induced by microwaves. *Carbon* **2010**, *48* (4), 1146−1152.

(29) Degioanni, S.; Jurdyc, A. M.; Cheap, A.; Champagnon, B.; Bessueille, F.; Coulm, J.; Bois, L.; Vouagner, D. Surface-enhanced Raman scattering of amorphous silica gel adsorbed on gold substrates for optical fiber sensors. *J. Appl. Phys.* **2015**, *118* (15), 153103.

(30) Mulder, C.; Damen, A. The origin of the "defect" 490 cm-1 Raman peak in silica gel. *J. Non-Cryst. Solids* **1987**, *93* (2−3), 387−394.

(31) Rich, S. I.; Wood, R. J.; Majidi, C. Untethered soft robotics. *Nat. Electron* **2018**, *1* (2), 102−112.

(32) Kitamori, T.; Wada, A.; Nabae, H.; Suzumori, K. Untethered three-arm pneumatic robot using hose-free pneumatic actuator. *2016 IEEE/RSJ International Conference on Intelligent Robots and Systems (IROS)*; Daejeon Convention Center, Daejeon, Korea, October 9−14, 2016. DOI: 10.1109/IROS.2016.7759106.

(33) Han, J.; Jiang, W.; Niu, D.; Li, Y.; Zhang, Y.; Lei, B.; Liu, H.; Shi, Y.; Chen, B.; Yin, L.; Liu, X.; Peng, D.; Lu, B. Untethered Soft Actuators by Liquid-Vapor Phase Transition: Remote and Programmable Actuation. *Advanced Intelligent Systems* **2019**, *1* (8), 1900109.

(34) Li, Y.; Chen, Y.; Ren, T.; Li, Y.; Choi, S. H. Precharged Pneumatic Soft Actuators and Their Applications to Untethered Soft Robots. *Soft robotics* **2018**, *5* (5), 567−575.

(35) Tolley, M. T.; Shepherd, R. F.; Karpelson, M.; Bartlett, N. W.; Galloway, K. C.; Wehner, M.; Nunes, R.; Whitesides, G. M.; Wood, R. J. An untethered jumping soft robot. *2014 IEEE/RSJ. International Conference on Intelligent Robots and Systems*; Chicago, IL, Sept. 14−18, 2014; pp 561−566. DOI: 10.1109/IROS.2014.6942615.

(36) Shaygan Nia, A.; Rana, S.; Döhler, D.; Noirfalise, X.; Belfiore, A.; Binder, W. H. Click chemistry promoted by graphene supported copper nanomaterials. *Chemical communications (Cambridge, England)* **2014**, *50* (97), 15374−15377.

(37) Shaygan Nia, A.; Rana, S.; Döhler, D.; Jirsa, F.; Meister, A.; Guadagno, L.; Koslowski, E.; Bron, M.; Binder, W. H. Carbon-Supported Copper Nanomaterials: Recyclable Catalysts for Huisgen 3 + 2 Cycloaddition Reactions. *Chemistry (Weinheim an der Bergstrasse, Germany)* **2015**, *21* (30), 10763−10770.

(38) Tripathi, S.; Bose, R.; Roy, A.; Nair, S.; Ravishankar, N. Synthesis of Hollow Nanotubes of Zn2SiO4 or SiO2:Mechanistic Understanding and Uranium Adsorption Behavior. *ACS Appl. Mater. Interfaces* **2015**, *7* (48), 26430−26436.

(39) Stober, W.; Fink, A.; Bohn, E. Controlled Growth of Monodisperse Silica Spheres in the Micron Size Range. *J. Colloid Interface Sci.* **1968**, *26* (26), 62−69.

(40) Schütt, F.; Signetti, S.; Krüger, H.; Röder, S.; Smazna, D.; Kaps, S.; Gorb, S. N.; Mishra, Y. K.; Pugno, N. M.; Adelung, R. Hierarchical self-entangled carbon nanotube tube networks. *Nat. Commun.* **2017**, *8* (1), 1215.

(41) Mishra, Y. K.; Kaps, S.; Schuchardt, A.; Paulowicz, I.; Jin, X.; Gedamu, D.; Freitag, S.; Claus, M.; Wille, S.; Kovalev, A.; Gorb, S. N.; Adelung, R. Fabrication of Macroscopically Flexible and Highly Porous 3D Semiconductor Networks from Interpenetrating Nano-

structures by a Simple Flame Transport Approach. *Part. Part. Syst. Charact.* **2013**, *30* (9), 775−783.

(42) Mishra, Y. K.; Modi, G.; Cretu, V.; Postica, V.; Lupan, O.; Reimer, T.; Paulowicz, I.; Hrkac, V.; Benecke, W.; Kienle, L.; Adelung, R. Direct Growth of Freestanding ZnO Tetrapod Networks for Multifunctional Applications in Photocatalysis, UV Photo-detection, and Gas Sensing. *ACS Appl. Mater. Interfaces* **2015**, *7* (26), 14303−14316.